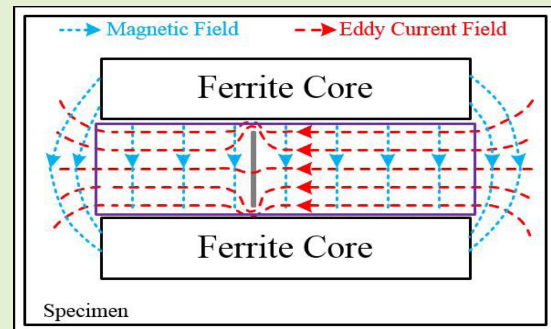


Microcracks Detection Based on Shuttle-Shaped Electromagnetic Thermography

Xiaofeng Li, Bin Gao¹, Senior Member, IEEE, Zewei Liu, and Gui Yun Tian², Senior Member, IEEE

Abstract—Nondestructive testing for natural microcracks is a critical challenge in assessing the surface and subsurface integrity of material. This paper proposes a shuttle-shaped sensing model with wide open inspection based on eddy current pulsed thermography (ECPT) system for natural microcrack detection on the specimens with complex geometry. To decrease the noise interference caused by uneven heating, the proposed model induces a unidirectional and uniform electromagnetic field in the region of interest. It significantly enhances thermal contrast and signal-to-noise ratio between non-defective and defective areas as well as improving the detectability and adaptability to different subjects. Besides, the direction of the infrared camera with respect to the specimen is set parallel to the specimen, which benefits the collection of the thermal signal. Experiments for several conductive cracks are implemented to verify the detectability of the proposed model.

Index Terms—Induction thermography, crack detection, complex workpiece, uniform eddy current field.



I. INTRODUCTION

IN the modern industrial field, for variety workpieces, especially in that having the strict standard on the process of production and usage, reliability and safety are of considerable importance [1], [2]. Nondestructive testing and evaluation (NDT&E) is a typical efficient detecting method to monitor and diagnose the material physical characteristics. It has been widely implemented in both science and industry without affecting the serviceability of the determinand [3], [4].

There are several NDE methods for natural crack detection, including Magnetic Particle Testing (MT) [5], [6], Penetrant Testing (PT) [7], Ray Testing (RT) and Eddy Current Testing (ECT). MT is a sensitive way to detect surface and subsurface cracks. However, the procedure of MT is complicated and time-consuming. In addition, the surface of the subject requires pretreatment as well as cleaning after

detection [6]. PT is a direct inspection method to a surface crack. Nevertheless, the demands on the surface is high, and pollution is generated [8]. The results of RT are easy to be obtained. However, radiation is harmful to people in terms of long time serving. The induction technology, based on the electromagnetic field [9], [10], [19] i.e., ECT [11], magnetic flux leakage (MFL), alternating current field measurement (ACFM) [12] and eddy-current pulse-compression thermography, has an essential superiority in NDT&E because the electromagnetic distribution can be easily affected by the defects. Yi *et al.* achieved quantitative evaluation of crack of depths on CFRP materials and thin aluminum plate using eddy current pulse-compression thermography [13]–[15]. Malekmo-hammadi *et al.* made an experimental comparison of LED and eddy current pulse-compression thermography on CFRP [16]. ECT is the most widely adopted testing method in electromagnetic NDT&E techniques [17]–[19]. As the probe has no need to contact the surface of the specimen, ECT is available for subsurface with wet films or coating. However, the lift-off variation and the shape of the probe have a significant impact on the testing results. Foudaz *et al.* [20] integrated the microwave with thermography and applied them to structural health inspection. Yang *et al.* [21] utilized the S-Band sensing technique to obtain the information of body motions in a wireless way and evaluate the cerebellar dysfunction. Yang *et al.* [22] used the C-Band sensing technique to monitoring the health status by capturing breathing-induced chest movements.

Infrared thermography (IRT) has been employed in NDT&E technology since its broad applicability [23], [24].

Manuscript received May 12, 2020; revised May 31, 2020; accepted June 7, 2020. Date of publication June 12, 2020; date of current version October 2, 2020. This work was supported in part by the National Natural Science Foundation of China under Grant 61971093, Grant 61527803, and Grant 61960206010, in part by the Science and Technology Department of Sichuan, China, under Grant 2019YJ0208, Grant 2018JY0655, and Grant 2018GZ0047, and in part by the Fundamental Research Funds for the Central Universities under Grant YGX2019J067. The associate editor coordinating the review of this article and approving it for publication was Dr. Qammer H. Abbasi. (Corresponding author: Bin Gao.)

Xiaofeng Li, Bin Gao, and Zewei Liu are with the School of Automation Engineering, University of Electronic Science and Technology of China, Chengdu 611731, China (e-mail: bin_gao@uestc.edu.cn).

Gui Yun Tian is with the School of Engineering, Newcastle University, Newcastle upon Tyne NE1 7RU, U.K.

Digital Object Identifier 10.1109/JSEN.2020.3001305

Eddy current pulsed thermography [25], [26] is a multi-physical coupling NDT&E method for conductive materials. It combines the measurement principles of magnetism, eddy current, Joule heat and infrared thermography. The material characteristics, such as electrical conductivity, magnetic permeability and thermal conductivity, can affect the induced electromagnetic field. Moreover, various kinds of cracks like structural deformation caused by crash, fatigue or scratch are legibly recorded and demonstrated in the thermal images. These can be validated by Joule heating via eddy current, heat transmission and infrared thermography. This technique can be expanded to other fields such as inductive heating [27].

The ferrite materials have been validated to concentrate the induced electromagnetic field on the area of interest in ECPT [28], [29]. Thus, the induced eddy current will enhance the temperature of the crack region and can be further identified within the process of thermal images. An L-shaped ferrite model ECPT is validated to offer an open inspection and concentrated and uniform electromagnetic field [30]. Besides, the recipe of the ferrite material can be adjusted to adapt to the subject, which leads to a better induction effect.

The distribution of inducted electromagnetic field can be determined by the configuration of the ECPT, so as the magnetic field intensity and electric current density. The signal-to-noise ratio (SNR) and testing sensitivity of ECPT is affected by the intensity and uniformity of the electromagnetic field around the crack area. Hence, there are several studies focused on identifying the factors affecting detection performance. These are the optimization of the excitation parameters by changing the induction material, improving sensing structure size and adjusting the observation angle [31]. Tsopelas *et al.* [32] evaluated the influence of the tilt angle of the exciting coils and found the factors in affecting the uniformity of the induced field by changing the lift-off distance and the position of the cross-sectional area of the coil. He *et al.* [33] proposed a ferrite-yoke induction probe to produce a relatively uniform eddy current field without blocking for quantitative defect evaluation. Hansen *et al.* [34] offered an asymmetric inductor to achieve uniform heating. However, the issues of low adaptability to different samples, limited detection area and low detection sensitivity in ECPT are challenging for defects identification. In particular, detections of various defects such as Rolling Contact Fatigue (RCF) Cracks [35], crevice existed in the welding line and the screw joints are all important since they give rise to unserviceability. Besides, the lift-off distance and geometry of the specimen have an enormous influence on the current density and distribution in the samples, which leads to false alarm [36], [37].

This paper proposed a shuttle-shaped induction structure of the electromagnetic-thermal ECPT by constructing shuttle-shaped wider open ferrite core with coil winding. This structure can improve the detectability of microcracks on the complicate surface of both ferromagnetic and non-ferromagnetic material. In this model, most of the inducted magnetic lines concentrate in the wide-open region of interest (ROI), where the electromagnetic field can be considered to be an approximately uniform distribution. Therefore, the sensitivity of detection can be relatively improved.

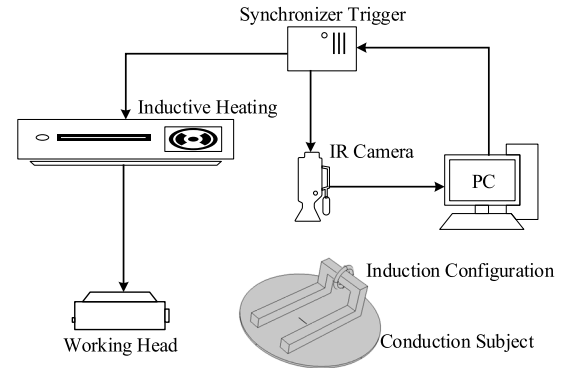


Fig. 1. The proposed configuration of ECPT system.

In addition, the ROI is entirely in the open view of the infrared camera while the region size is more sufficient to illustrate the difference between the crack and other regions. The detection capability of the proposed model has been validated through both simulation and experiments.

The rest of this paper is demonstrated as follows. Section II presents the theoretical and simulation model of the proposed configuration. Section III offers the simulations and experiment results. Conclusions and future works are summarized in Section IV.

II. METHODOLOGY

A. Detection Configuration of ECPT

The new configuration of ECPT is proposed and demonstrated in Fig. 1. In particular, the excitation configuration is made of wide-open inspection ferrite core and copper helix coil. When the controller sends a signal to start the testing, pulsed high-frequency current is generated and flows through the helix coil. The alternating magnetic flux is generated. In the electromagnetic field, the induced eddy current intensity and thermal transmission will be affected if the crack exists in the sample. Hence, the transient time-spatial characteristics of the Joule heat can be recorded by the infrared camera.

B. Mathematical Models of Electromagnetic Field

Fig. 2 illustrates the schematic diagram of the magnetic flux path. The magnetic flux can be divided into three interpretations. Part I represents the magnetic flux generated by the coil, it flows into the air and the ferrite core. One of the magnetic flux paths in the air can be marked with the blue dotted line. Part II illustrates the magnetic flux that flowed through the ferrite core and air between the two legs. One of the magnetic flux paths in the core is marked with the yellow dotted line and one of the magnetic flux paths that flowed through the air is marked with the green dotted line. Part III represents the magnetic flux that flowed through the sample. Part of the paths in the sample is represented by the red dotted line.

The relationship between magnetic flux and the magnetic resistance can be illustrated as follows [38]:

$$mmf = NI = \emptyset R \quad (1)$$

where mmf is the magnetic motive force, which is generated by the current I in the coil with N turns, \emptyset denotes the

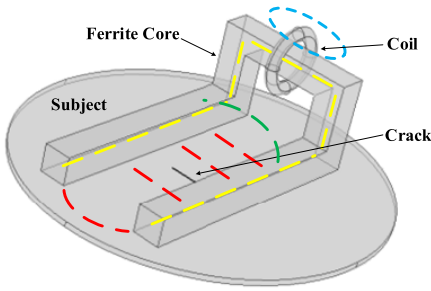


Fig. 2. The magnetic flux path of the structure.

magnetic flux and R is the reluctance of a magnetic circuit. Furthermore, the reluctance can be represented as follows [30]:

$$R_i = \frac{l_i}{\mu_i A_i} \quad (2)$$

where R_i is the reluctance in each part, l_i is the average length of the path, μ_i represents the permeability of the material and A_i denotes the sectional area of each path.

In this proposed configuration, the permeability of the core holds $\mu_c \gg \mu_s$, $\mu_c \gg \mu_0$, where μ_s represents the permeability of the subject and μ_0 denotes the permeability of the air. For ferromagnetic material specimen, $\mu_s \gg \mu_0$, and for the nonferromagnetic material specimen, $\mu_s = \mu_0$. The reluctance of the ferrite core can be assumed as 0 because of its high permeability.

For ferromagnetic material, because of its high permeability and low reluctance, a majority of magnetic flux flow through the specimen. Meanwhile, the magnetic flux is distributed on the surface of the subject because of the small skin depth. The skin depth δ can be calculated by [39]:

$$\delta = \frac{1}{\sqrt{f\pi\mu\sigma}} \quad (3)$$

where the f is the frequency of the excitation current, μ is the permeability and σ is the electrical conductivity. However, for nonferromagnetic material, the specimen has no effect on the distribution of the magnetic field in account of the inexistence of the magnetic domain. Thus, for nonferromagnetic material, the magnetic flux that flowed through the specimen decreases with the lift-off distance increasing.

When the shape of the ferrite core changes, the reluctance of the ferrite core will change strongly since the different length of the magnetic flux path into sectional area. In addition, the saturation magnetic flux increases with the volume of core increasing. The magnetic flux that flowed into the ferrite core increases along with the driving power until it reaches the saturation point. The more magnetic flux is generated, the stronger the induced eddy current field is.

The shuttle-shaped ferrite core guides a large proportion of the magnetic flux into the specimen and the distribution of electromagnetic field on the region of interest is uniform. In addition, the magnetic flux that leaked into the air has rare effect on the distribution of the eddy current field in the sample.

For the microcrack testing, the variational magnetic field leads to stable and uniform eddy current field in the specimen

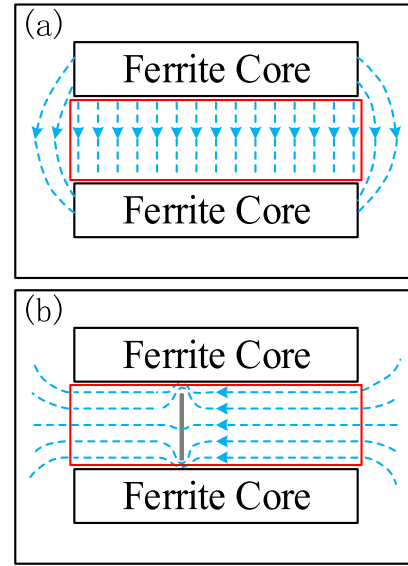


Fig. 3. Distribution of magnetic field and induced eddy current field.

so that the infrared camera could catch the thermal abnormality that caused by the defect. In addition, the skin depth determines the induced eddy current density on the surface. Thus, the selection of frequency has a significant effect on the detection performance while the amplitude of the magnetic flux density has an upper limit. The excitation frequency in this configuration is set as several hundred kHz to achieve the small skin depth. The displacement eddy current density can be neglected in this frequency range.

After setting the boundary conditions of the detection model, the distribution of the magnetic field and eddy current field can be calculated by using finite element method (FEM). The distribution of the magnetic field and the induced eddy current field on the surface are demonstrated in Fig. 3. The area within the red line marked area is the region of interest. The distribution of the magnetic field is illustrated in Fig. 3(a), and the direction of induced eddy current field is vertical to the magnetic field's. The electromagnetic field in the ROI is relatively homogeneous, which is an extremely advantageous condition for detecting superficial crack.

If crack exists in the region of inspection, the uniform eddy current field will be disorganized, as shown in Fig. 3(b). The eddy current tends to bypass the crack in a shorter path. Therefore, the highest current density will appear in the tips and bottom of the crack.

C. Joule Heating Analysis and Ferrite Material

As there exists resistance in metal materials, the induced eddy current generates heat inside the subject. The Joule heat effect calculates the thermal field with eddy current field. This relationship between the Joule heat Q and eddy current field intensity vector E can be illustrated as follows [40]:

$$Q = \frac{1}{\sigma} |J|^2 = \frac{1}{\sigma} |\sigma E|^2 \quad (4)$$

where the σ denotes the electrical conductivity.

By taking account of Joule heat and heat diffusion, the temperature distribution can be denoted by:

$$\frac{\partial T}{\partial t} = \frac{K}{\rho C_p} \left(\frac{\partial^2 T}{\partial x^2} + \frac{\partial^2 T}{\partial y^2} + \frac{\partial^2 T}{\partial z^2} \right) + \frac{1}{\rho C_p} q(x, y, z, t) \quad (5)$$

where $T = T(x, y, z, t)$ represents the distribution of temperature, K is the thermal conductivity of the subject, ρ denotes the density, C_p means the specific heat capacity, $q(x, y, z, t)$ denotes the generated internal heat per unit volume and per unit time, which is caused by the Joule heating.

As can be seen from Eq.(5), the generated Joule heat will spread from the higher temperature area to the lower region. Due to the uniform distribution of the electromagnetic field, for ferromagnetic material, the Joule heat is produced uniformly within the ROI. For nonferromagnetic material, the heat is generated inside the sample where the induced current exists. With the area of ROI increasing, the energy decreases for every unit area.

When there exists a crack in the ROI, the area near the crack generates more heat on account of its higher eddy current density. Therefore, the temperature near the crack is higher than other place during the heating stage. In addition, the horizontal thermal transmission will be blocked in the defect edge due to the sudden decrease of the heat transfer. The temperature is spreading from the surface of the specimen to the subsurface, which is termed as vertical thermal diffusion. Consequently, part of the heat concentrates on the tips or bottom of the crack in the cooling stage, and this characteristic can be utilized for detecting omnidirectional cracks.

The formulation of ferrite materials will affect the critical parameters such as the initial permeability, the power loss and the saturation flux density, which is important for induction effect. For example, the material of PC44 is used in this submission, and its main formulation is Fe2O3 : MnO : ZnO = 53.5 : 36.5 : 10 in mole fraction. The increase of the percentage of Fe2O3 leads to the increase of the saturation flux density. The increase of the percentage of ZnO results in the decrease of the Curie temperature and the increase of the initial permeability. In addition, the small amounts of additives could affect the material properties, i.e. MoO and CuO.

D. Infrared Radiation and Field of Observation

Once the temperature of any object is above absolute zero, the object will continuously absorb or emit electromagnetic radiation, mainly infrared radiation, due to the motion of charged particles. The radiant intensity I represents the radiant power emitted from a point source in the object [41]:

$$I = I_0 \cdot \cos\theta \quad (6)$$

where I_0 denotes radiation intensity in the perpendicular direction of the surface, θ is the angle between the observing direction and normal direction of the surface. Thus, the camera could catch the complete thermal information only if the θ equals 90-degree, which means a higher possibility of identifying the defect. Therefore, putting the infrared camera right on the ROI benefits the detection.

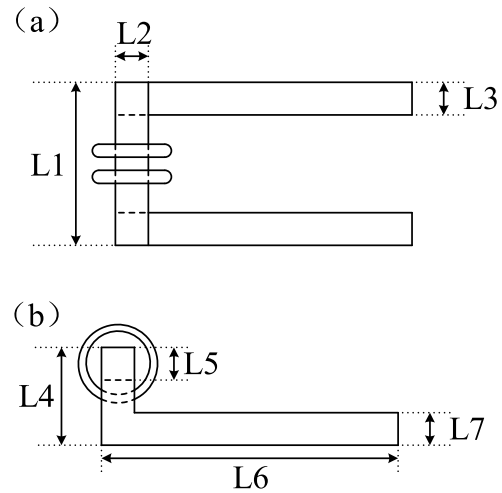


Fig. 4. The (a) top view (b) side view of the configuration.

TABLE I
DIMENSIONS OF THE EXCITATION CONFIGURATION

Parameters	L1	L2	L3	L4	L5	L6	L7
Values(mm)	65	15	15	42	15	75	12

The proposed configuration offers such a broad, obstructed view so that the entire thermal signal of the ROI can be captured to benefit the detection performance.

III. EXPERIMENT VALIDATION

A. Simulation Experiment and Results

For the purpose of validating the electromagnetic and heating characteristics of the proposed configuration, several finite element simulation models are created. All simulation experiments for crack detection on a plate and a column with the complex geometric structure are adopted by the induction heating models of the COMSOL Multiphysics simulation platform.

The general view of the simulation configuration is shown in Fig. 4. The top view of the structure is represented in Fig. 4(a) and the side view is represented in Fig. 4(b). Besides, the helix coil is made of copper and the ferrite material is applied. The dimensions of the configuration are demonstrated in Table I. The radius of the helix copper coil with two turns equals 12 mm and the diameter of the copper pipe is 4 mm. In simulation, the magnitude and frequency of the current in the coil are set as 200A and 200kHz, respectively. The initial temperature value equals 293.15k.

The distribution of the electromagnetic field in the ROI of the non-defective subject has been calculated. The simulation performance of various orientation cracks and different lift-off distances in both ferromagnetic and nonferromagnetic subjects have been validated. In particular, the simulations for both ferromagnetic and nonferromagnetic subjects with complex geometry have been accomplished. To get close to the actual application, we choose 45# steel and 316# stainless

TABLE II
MATERIAL PARAMETERS

Parameters	copper	ferrite	316#	45#
Conductivity (S/m)	5.998e7	1e-6	1.3e6	5.5e6
Relative permeability	1	2000	1	190
Density (kg/m ³)	8700	7800	7990	7850
Heat capacity (J/(kg K))	385	600	502	475
Thermal conductivity (W/(m K))	400	5	12.1	51.9

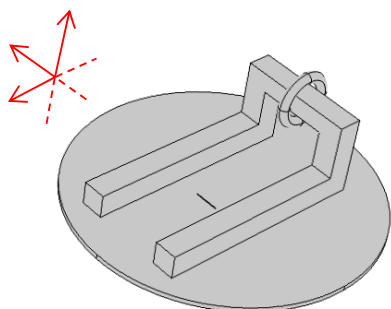


Fig. 5. Space diagram and the direction of x, y, z.

steel as the materials of test plate. The material parameters settings including conductivity, relative permeability, density, heat capacity and thermal conductivity which are listed in Table II. It should be noted that the change of permeability caused by the temperature change can be neglected since the temperature is far below the Curie temperature.

1) *The Simulation Experiment for the Distribution of Electromagnetic Field in the ROI*: The space diagram of the model with the Cartesian coordinate system is illustrated in Fig. 5. A non-defective rectangle metal plate with 180mm length, 150mm width and 8mm thickness is implemented for the simulation experiments. Fig. 6 shows the distribution of the electromagnetic field on the plate surface without a defect. The ROI is outlined with solid line. Within the ROI, the red arrows represent the magnetic field and the blue arrows represent the eddy current field. As can be seen apparently, almost all arrows of the electromagnetic field point to the same direction as well as same amount. Thus, it can be concluded that a relatively uniform electromagnetic field is induced in the ROI.

2) *The Defect Detection of Plate*: Fig. 7 is the top view of the simulation model. This figure represents the relative position between the excitation configuration and the specimen. Since the natural cracks are small, the measure of the crack is set as length \times width \times depth = 3mm \times 0.3mm \times 0.3mm. To validate the detectability to different orientation cracks, we choose four different angles, which are set at 0°, 30°, 60° and 90°,

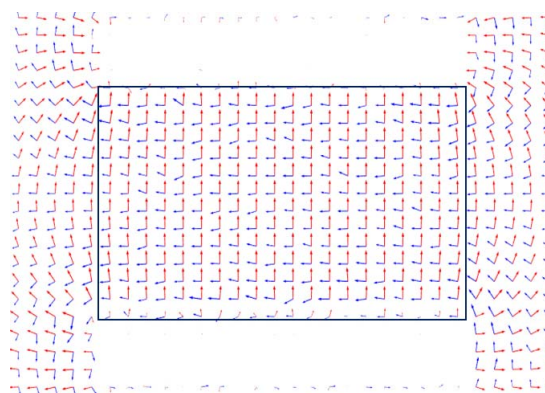


Fig. 6. Magnetic flux vectors and induced eddy current vectors without defect in the ROI.

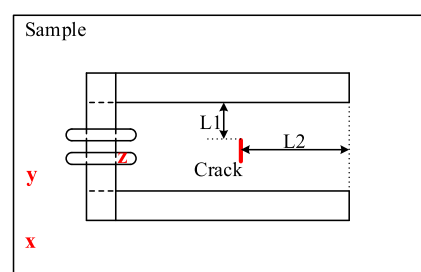


Fig. 7. The top view of the detection model.

respectively. The L1 equals to 16mm and the L2 equals to 30mm, which means the crack exists in the middle of ROI that benefits the detection and inspection.

The simulation results of multiple orientation cracks are shown in Fig. 8. The temperature distribution of 45# steel and 316# stainless steel with different orientation cracks are presented which interprets that there exists a high temperature around the cracks. Moreover, it should be noted that the phenomenon of high temperature is weakened with the angle increasing. The distribution of temperature on the surface depends on the different disturbance of the electromagnetic field caused by different angle cracks. Since the relative permeability of 316# stainless steel is the same as the air, the perturbation of the magnetic field caused by various orientation cracks is slight. Thus, the simulation performance of 316# stainless steel depends on the disturbance of eddy current. Hence, different orientation cracks on 45# steel and all the cracks, which are not parallel to the legs of ferrite core, of 316# stainless steel can be detected by the proposed configuration.

The thermal contrast (TC) and absolute temperature rise (ΔT) of the simulation performance under different lift-off distance is demonstrated in Table III. According to the quantitative results, all defects in both 45# steel and 316# stainless steel have shown high TC values. It is evident that the values of TC and ΔT decrease sharply while the lift-off change from 4mm to 7mm in contrast to the others. This indicates that the proposed model has a range of lift-off distance that can assure good results.

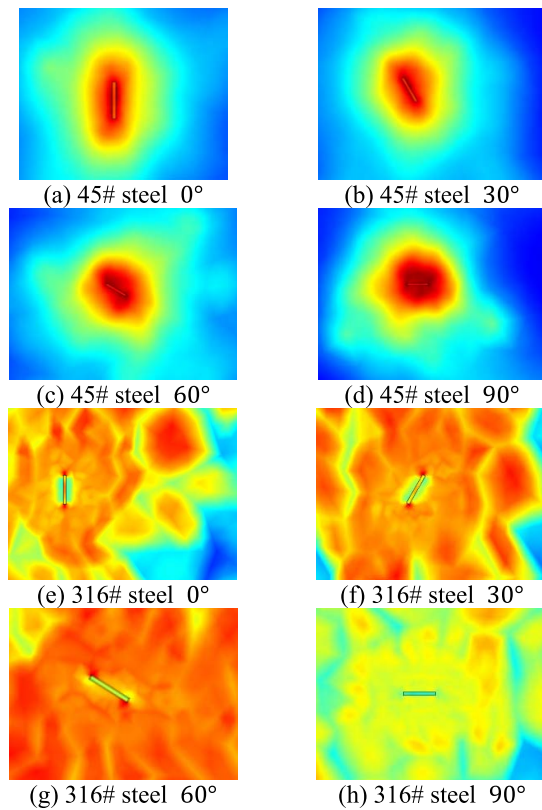


Fig. 8. The results of 45# steel and 316# stainless steel.

TABLE III
THE TC AND ΔT UNDER DIFFERENT LIFT-OFF DISTANCE

		1mm	4mm	7mm	10mm
45#	ΔT (K)	18.61	17.88	8.23	7.24
	TC (%)	922%	882%	352%	298%
316#	ΔT (K)	0.96	0.91	0.81	0.70
	TC (%)	200%	184%	153%	119%

3) *The Detection of Complex Geometry*: The subject with complex geometry and the simulation results are presented in Fig. 9. The crack is placed close to the joint of two cylinders. In addition, the shape of the defect is a small cube with 0.4mm length, 0.4mm width and 0.2mm depth. The 3D model for detecting the subject with complicated geometry is illustrated in Fig. 9(b).

Fig. 9(c) and (d) represent the temperature distribution on the surface of the sample with complex geometry. Fig. 9 is the result of #316 stainless steel. The distinct temperature change occurred near the crack. The same situation happened in the result of the defective surface of 45# steel in Fig. 9(d). The TC values of the detection results of complex geometry are presented in Table IV. Due to the high thermal contrast, the detectability of the proposed configuration is validated.

B. Experimental Verification

In order to verify the practicability of the proposed configuration, experiments are implemented. The detection system

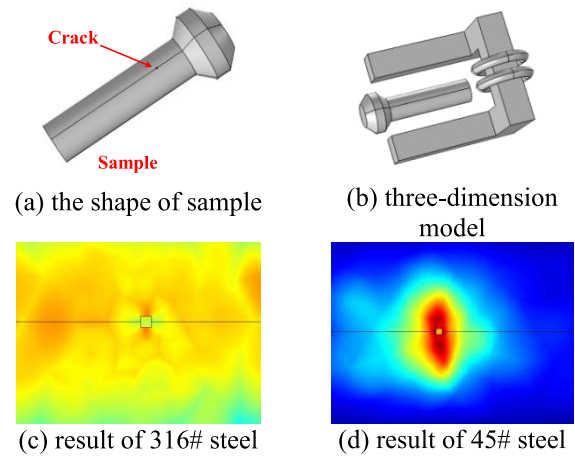


Fig. 9. The results of complex structure.

TABLE IV
THE TC OF THE RESULTS OF COMPLEX GEOMETRY

	45# steel	316# stainless steel
TC	439%	138%

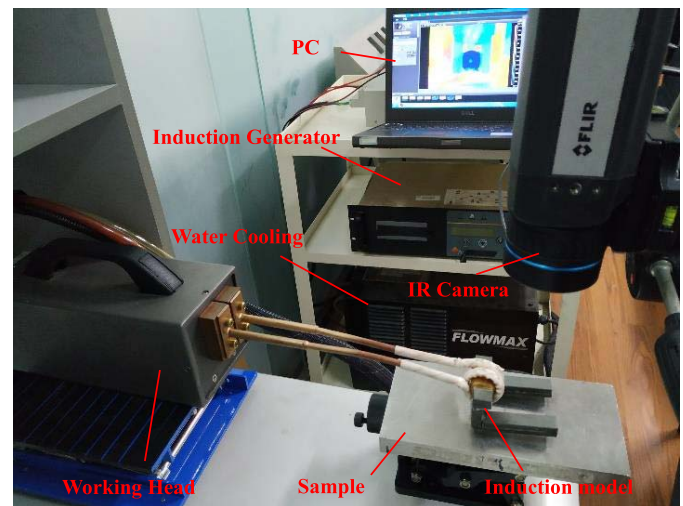


Fig. 10. The proposed ECPT system.

is shown in Fig. 11. The high-frequency power generator, Easyheat 224, and cooling device are applied for excitation. The infrared camera is Flir SC655 with the 640*120 resolution and 200Hz max frame rate. The thermal sensitivity of the camera is below 50mK. The inductance of the ferrite core winding two turns helix coil is 1uH. In these experiments, the excitation frequency is matched around 200kHz. The current is set as 200A to provide sufficient power to generate heat, and the heat-up time is set as 200ms. Experimental studies focused on natural cracks of several specimens with various complex surface conditions for the purpose of validating the detectability and reliability of the proposed structure. Furthermore, the contrast tests achieved by the line-coil ECPT

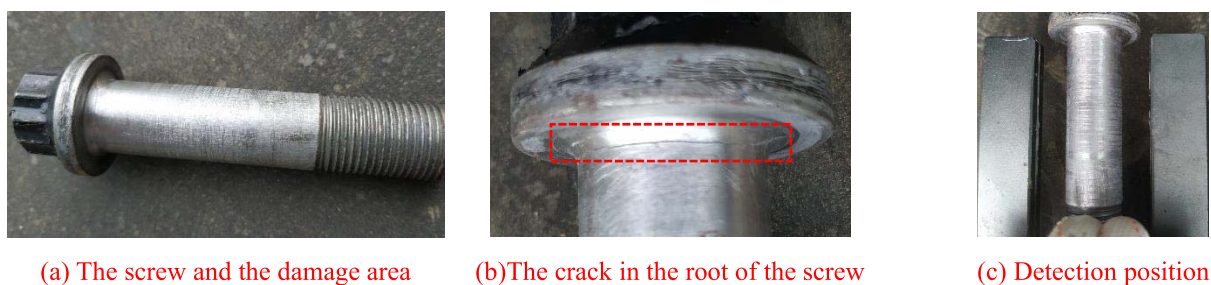


Fig. 11. The crack in the root of the screw.

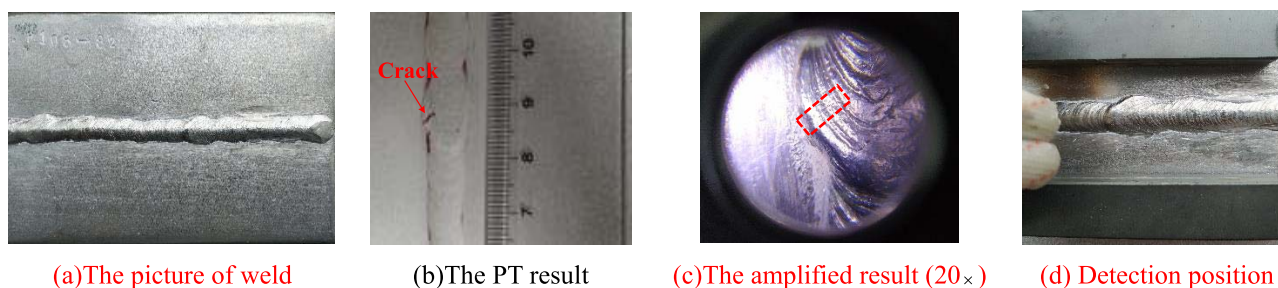


Fig. 12. Description of weld specimen and the surface natural crack.

system, helix-coil ECPT system and L-shaped ECPT system are the assisted validation.

1) *Description of Specimen*: The screw subject with a complex surface is shown in Fig. 11(a). The natural fatigue microcrack is located at the root of the screw, which is marked by the red line, as illustrated in Fig. 11(b). It can be seen that the crack is exceptionally narrow and irregular. Since the defect is close to the edge and the inspection can be blocked, the detection is inconvenient and challenging to be performed with conventional configuration based on the ECPT system.

The overview of the weld subject is shown in Fig. 12 (a). In order to validate the accuracy of detection results, the penetration testing (PT) for this specimen is conducted in advance, and the PT result is illustrated in Fig. 12(b). The natural crack in the welding line is formed from the welding stage and unpredictable. Meanwhile, it is too small and snatchy to be observed while the surface condition of the welding line suffers a significant interference. Fig. 12(c) is the 20 times magnified picture of the crack, and it shows the characteristics of thin, intermittent and irregular of the crack. Hence, the thermal distribution will be changed since the existence of the crack hinders the eddy current field.

The rail sample with rolling contact fatigue cracks is described in Fig. 13(a). In this experiment, the inductor is placed over the specimen surface and the ROI covers the nearly whole surface as shown in Fig. 13(b) so that all cracks in the ROI can be recognized.

The stainless steel subject and its magnetic particle testing (MT) detection result are illustrated in Fig. 14(a). The natural stress corrosion microcrack exists in the subsurface of the subject. Fig. 14(a) shows that the defect is discontinuous and irregular. The defect area was marked with the red rectangle. Due to the surface of the stainless steel subject is polished in advance and the crack is subsurface stress

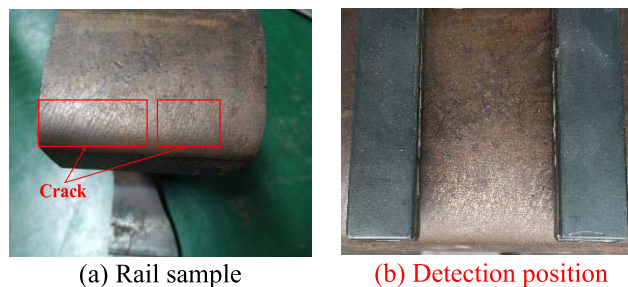


Fig. 13. Rail sample and the detection position.

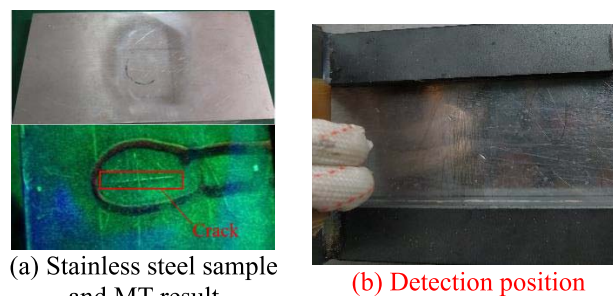


Fig. 14. The stainless steel sample.

corrosion defect, the high light reflection is a distraction as shown in Fig. 14(c).

In the contrast experiments, the radius and pipe diameter of the helix-coil with three turns are 22 mm and 6 mm, respectively. The pipe diameter of the line-coil is 6mm. The excitation current for all contrast experiments is set as 200A, 200kHz. The relative position between the subjects and the excitation configuration is shown in Fig. 15. The excitation configurations are placed near the crack. The lift-off distance

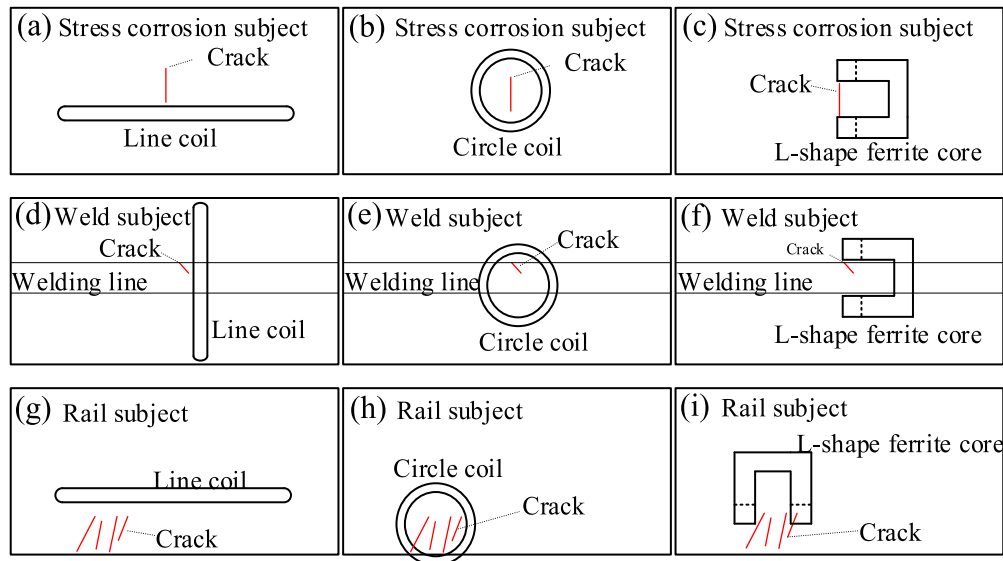


Fig. 15. The top view of detection models. (a)(b)(c) stress corrosion subject detection (d)(e)(f) Weld subject detection (g)(h)(i) Rail detection.

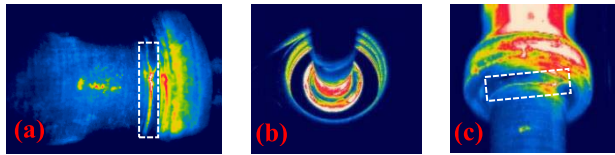


Fig. 16. The experiment results of screw using (a) L-shape model (b) helix-coil (c) proposed model.

between the excitation configurations and subjects are 5mm. The screw subject is placed in the middle between the two legs of the ferrite core.

The frame rate is set as 200Hz for the FLIR infrared camera with a 640×240 array is used to accomplish the validation experiments.

2) Results Analysis:

a) *Detection results of screw fatigue crack:* The verified experiments are achieved by using the L-shaped excitation configuration to detect the fatigue cracks in the root of screws which is shown in Fig. 16(a). Fig. 16(b) indicates that the strong noise can cover the crack signal. In contrast to the other results, Fig. 16(c) shows that the cracks are detected with high-temperature contrast and the outline of the crack is clearly presented. Furthermore, the inspection brought from the proposed model is more comprehensive than the L-shape model. This indicates that the proposed excitation model can effectively detect natural microcracks in screws.

b) *Detection results of weld crack:* Fig. 17(a) shows that a comparatively clear outline of the crack with intense noise. In the comparison tests, Fig. 17(b) is the detection result by using line-coil and Fig. 17(c) is the detection result by using helix-coil. As can be seen from Fig. 17(b), there exists sharp noise around the crack and it is hard to be detected. In Fig. 17(c), part of crack can be seen. However, the noise signal below the coil is strong as well. The experiment result by using the proposed configuration is demonstrated in Fig. 17(d). The outline of the crack is clear to be recognized

and the thermal image illustrates that the cracks disturb the electromagnetic field. The scales on the welding line are so intensive and extensive that they generate tremendous thermal signals to cover up the signal of crack through the thermal diffusion. Obviously, the proposed model can deduce the power distributed on the scales through heating a wide area and emerge the outline of crack.

c) *Detection results of rolling contact fatigue cracks:* Fig. 18 shows the detection results of rolling contact fatigue cracks, which disclose the presence of cracks at the edge of the rail surface. The outline of the cracks in the ROI is clearly presented through the higher temperature contrast. These contrasts experiments show the detectability and full inspection of the proposed excitation model in detecting multiple defects.

d) *Detection results of subsurface intergranular stress corrosion defect:* Fig. 19 represents the detection results of the subsurface intergranular corrosion defect in stainless steel plate. It should be noted from Fig. 19(d) that the high-temperature points are distributed intermittent, which is a representative performance of natural crack caused by stress corrosion. According to the testing results, it can be validated that the proposed configuration has a strong detectability to identify the stress corrosion crack on the subsurface stainless steel plate.

As can be seen from the figures 16-19, the proposed model has two prominent advantages. For thermal image, the proposed model could heat the specimen surface in a short time so that the thermal image can present disorganized current field. The regions of high temperature are caused by the complex surface or the crack, which they can be easily distinguished. With the larger detection area, the more information of the surface is obtained to benefit the crack identification. In terms of thermal image processing, it would be easier to extract the crack information when the signal-to-noise ratio is improved.

In order to evaluate the detectability of the proposed structure from the quantitative perspective, the signal-to-noise ratio (SNR) of the detection results by using four different excitation models are calculated. The formula of SNR (dB) is represented

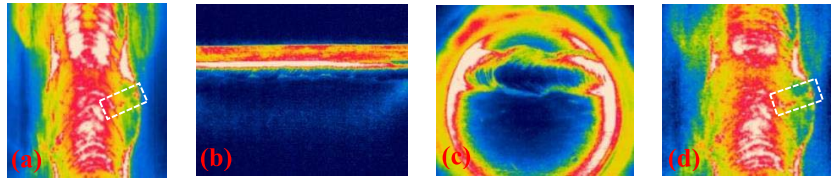


Fig. 17. The experiment results of weld cracks using (a) L-shape model (b) line-coil (c) helix-coil (d) proposed model.

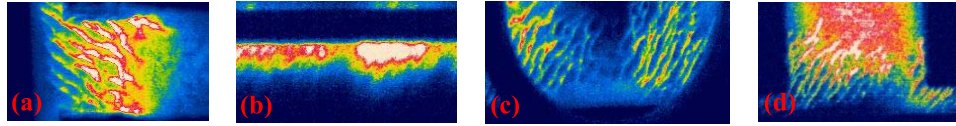


Fig. 18. The experiment results of RCFs using (a) L-shape model (b) line-coil (c) helix-coil (d) proposed model.

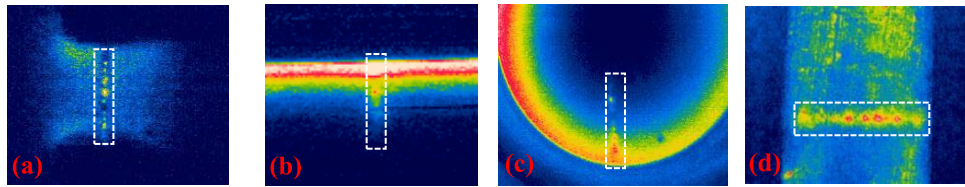


Fig. 19. The experiment results of the stainless steel plate using (a) L-shape model (b) line-coil (c) helix-coil (d) proposed model.

TABLE V
THE SNR (dB) OF DEFECT DETECTION EXPERIMENTS

	Screw	weld	RCFs	stainless steel
line-coil	--	×	2.63	0.61
helix-coil	×	1.16	5.85	2.03
L-shape model	7.203	4.43	8.81	15.87
Proposed model	15.56	7.51	13.38	16.25

as follows:

$$SNR = 20 \log_{10} \left(\frac{T_D}{T_N} \right) [dB] \quad (7)$$

where T_D is the average temperature in the defective area and T_N denotes average temperature in the non-defective area.

The SNR quantitative results are recorded in Table V. The “×” means that the excitation model could not identify the microcrack, and the “--” means that the coil cannot be used to detect the sample. In the test of the screw sample, the line-coil is unable to detect the crack since the observation path is obstructed. As can be observed from the Table V that using the helix-coil to detect the screw subject leads to an unsatisfactory result, which exists the complex background and the disadvantageous view. The L-shaped model offers a relative good result. In contrast, the SNR of the proposed structure equals 15.56dB, which means that the microcrack in the screw can be identified easily. In the tests of the weld specimen, the results of the line-coil and helix-coil are unable to identify the crevice, and the SNR of the proposed structure improves by 3.08dB compared with L-shaped model. In the experiments of RCFs, the result of the proposed structure

have apparent superiority while the SNR of the proposed configuration leads to an improvement of 10.75dB for line-coil, 7.53dB for helix-coil and 4.57dB for L-shaped coil. Obviously, the inspection of the proposed model is more extensive than the L-shape model. In the experiments of stainless steel, the results show that the detectability of the proposed model is similar to the L-shaped model and much stronger than the others. In summary, compared to the pre-existing excitation models, the proposed configuration improves the detectability greatly by enhancing the thermal contrast and offering a wide inspection window. And the broad excitation region leads to heating uniformly and enhancing the detectability of microcracks in complex geometry.

IV. CONCLUSION AND FUTURE WORK

In this paper, a novel shuttle-shaped sensing ECPT system is validated for microcracks detection. The theoretical model of the excitation configuration is developed. The detection results of natural microcracks on several ferromagnetic and nonferromagnetic material specimens are analyzed. Several conclusions can be drawn as follows:

i) The proposed model can generate a wide uniform electromagnetic field. Once there exists a microcrack, the homogeneity of the electromagnetic field will be affected. The eddy current intensity of the defective region performs higher than of other region while it will generate more heat so that the microcrack can be captured with significant thermal contrast.

ii) The proposed excitation model offers a broad heating region of interest and high excitation efficiency since it can generate sufficient heat to identify the crack with less heating time. In addition, less heating time leads to weaker thermal noise so that the heat diffusion cannot affect the thermal signal of the crack.

iii) The proposed configuration provides an extensive inspection to detect a large area at once. Meanwhile, the infrared camera can perform signal collection in the optimal angle as well as acquiring the integral thermal signal to benefit the detection.

Future work will focus on the motion detection of natural microcracks under the complex surface condition and application in the inductive heating.

REFERENCES

- [1] J. Wilson, G. Y. Tian, I. Z. Abidin, S. Yang, and D. Almond, "Pulsed eddy current thermography: System development and evaluation," *Insight-Non-Destruct. Test. Condition Monit.*, vol. 52, no. 2, pp. 87–90, 2010.
- [2] J. Vrana and M. Goldammer, "Induction and conduction thermography: From the basics to application," in *Proc. Thermographie-Kolloquium*, 2017, pp. 1–47.
- [3] X. Huang, C. Yin, S. Dadras, Y. Cheng, and L. Bai, "Adaptive rapid defect identification in ECPT based on K-means and automatic segmentation algorithm," *J. Ambient Intell. Hum. Comput.*, vol. 2018, no. 7, pp. 1–18, Jan. 2018.
- [4] G. Y. Tian and Y. L. Gao, "Multiphysics integrated NDT&E and progress on eddy current pulsed thermography," in *Proc. Int. Workshop Electromagn. Nondestruct. Eval.*, 2016, p. 141.
- [5] N. Kasai, A. Takada, K. Fukuoka, H. Aiyama, and M. Hashimoto, "Quantitative investigation of a standard test shim for magnetic particle testing," *NDT & E Int.*, vol. 44, no. 5, pp. 421–426, Sep. 2011.
- [6] K. Fukuoka, S. Noma, M. Kobayashi, T. Ozaki, and Y. Oikawa, "Consideration of multi-coil type magnetizer for detection of omnidirectional crack in magnetic particle testing," *Int. J. Appl. Electromagn. Mech.*, vol. 52, no. 3, pp. 1–8, 2016.
- [7] G. M. Light, "X-ray fluorescence testing of laminate structures," U.S. Patent 4577337 A, Mar. 18, 1986.
- [8] R. Clark, "The effect of crack closure on the reliability of NDT predictions of crack size," *NDT & E Int.*, vol. 20, no. 5, pp. 269–275, Oct. 1987.
- [9] K. Miya, "Recent advancement of electromagnetic nondestructive inspection technology in Japan," *IEEE Trans. Magn.*, vol. 38, no. 2, pp. 321–326, Mar. 2002.
- [10] Z. D. Wang, Y. Gu, and Y. S. Wang, "A review of three magnetic NDT technologies," *J. Magn. Magn. Mater.*, vol. 324, no. 4, pp. 382–388, Feb. 2012.
- [11] M. Morozov, G. Y. Tian, and P. J. Withers, "Noncontact evaluation of the dependency of electrical conductivity on stress for various Al alloys as a function of plastic deformation and annealing," *J. Appl. Phys.*, vol. 108, no. 2, pp. 2211–8142, 2010.
- [12] M. P. Papaalias, M. C. Lugg, C. Roberts, and C. L. Davis, "High-speed inspection of rails using ACFM techniques," *NDT & E Int.*, vol. 42, no. 4, pp. 328–335, Jun. 2009.
- [13] Q. Yi, G. Y. Tian, H. Malekmohammadi, J. Zhu, S. Laureti, and M. Ricci, "New features for delamination depth evaluation in carbon fiber reinforced plastic materials using eddy current pulse-compression thermography," *NDT & E Int.*, vol. 102, pp. 264–273, Mar. 2019.
- [14] Q. Yi, H. Malekmohammadi, G. Y. Tian, S. Laureti, and M. Ricci, "Quantitative evaluation of crack depths on thin aluminum plate using eddy current pulse-compression thermography," *IEEE Trans. Ind. Informat.*, vol. 16, no. 6, pp. 3963–3973, Jun. 2020, doi: [10.1109/TII.2019.2943669](https://doi.org/10.1109/TII.2019.2943669).
- [15] Q. Yi *et al.*, "Evaluation of debonding in CFRP-epoxy adhesive single-lap joints using eddy current pulse-compression thermography," *Compos. B, Eng.*, vol. 178, Dec. 2019, Art. no. 107461.
- [16] H. Malekmohammadi, S. Laureti, M. Ricci, Q. Yi, J. Zhu, and G. Y. Tian, "An experimental comparison of LED and eddy current pulse-compression thermography on an impact damage CFRP benchmark sample," in *Proc. IEEE Far East NDT New Technol. Appl. Forum (FENDT)*, Jul. 2018, pp. 13–17, doi: [10.1109/FENDT.2018.8681968](https://doi.org/10.1109/FENDT.2018.8681968).
- [17] M. He, L. Zhang, W. Zheng, and Y. Feng, "Crack detection based on a moving mode of eddy current thermography method," *Measurement*, vol. 109, pp. 119–129, Oct. 2017.
- [18] O. Lucia, P. Maussion, E. J. Dede, and J. M. Burdío, "Introduction to the special section on induction heating systems," *IEEE Trans. Ind. Electron.*, vol. 61, no. 5, pp. 2504–2508, May 2014.
- [19] L. Ferrigno, M. Laracca, H. Malekmohammadi, G. Y. Tian, and M. Ricci, "Comparison of time and frequency domain features' immunity against lift-off in pulse-compression eddy current imaging," *NDT & E Int.*, vol. 107, Oct. 2019, Art. no. 102152, doi: [10.1016/j.ndteint.2019.102152](https://doi.org/10.1016/j.ndteint.2019.102152).
- [20] A. Foudazi, M. T. Ghasr, and K. M. Donnell, "Characterization of corroded reinforced steel bars by active microwave thermography," *IEEE Trans. Instrum. Meas.*, vol. 64, no. 9, pp. 2583–2585, Sep. 2015.
- [21] X. Yang *et al.*, "S-band sensing-based motion assessment framework for cerebellar dysfunction patients," *IEEE Sensors J.*, vol. 19, no. 19, pp. 8460–8467, Oct. 2019, doi: [10.1109/JSEN.2018.2861906](https://doi.org/10.1109/JSEN.2018.2861906).
- [22] X. Yang, D. Fan, A. Ren, N. Zhao, and M. Alam, "5G-based user-centric sensing at C-band," *IEEE Trans. Ind. Informat.*, vol. 15, no. 5, pp. 3040–3047, May 2019, doi: [10.1109/TII.2019.2891738](https://doi.org/10.1109/TII.2019.2891738).
- [23] B. Gao, W. L. Woo, Y. He, and G. Y. Tian, "Unsupervised sparse pattern diagnostic of defects with inductive thermography imaging system," *IEEE Trans. Ind. Informat.*, vol. 12, no. 1, pp. 371–383, Feb. 2016.
- [24] H. Zhang *et al.*, "Optical and mechanical excitation thermography for impact response in basalt-carbon hybrid fiber-reinforced composite laminates," *IEEE Trans. Ind. Informat.*, vol. 14, no. 2, pp. 514–522, Feb. 2018.
- [25] Y. He and R. Yang, "Eddy current volume heating thermography and phase analysis for imaging characterization of interface delamination in CFRP," *IEEE Trans. Ind. Informat.*, vol. 11, no. 6, pp. 1287–1297, Dec. 2015.
- [26] A. Yin, B. Gao, G. Y. Tian, W. L. Woo, and K. Li, "Physical interpretation and separation of eddy current pulsed thermography," *J. Appl. Phys.*, vol. 113, no. 6, Feb. 2013, Art. no. 064101.
- [27] O. Lucia, P. Maussion, E. J. Dede, and J. M. Burdío, "Induction heating technology and its applications: Past developments, current technology, and future challenges," *IEEE Trans. Ind. Electron.*, vol. 61, no. 5, pp. 2509–2520, May 2014.
- [28] J. Zhao, B. Gao, W. L. Woo, F. Qiu, and G. Y. Tian, "Crack evaluation based on novel circle-ferrite induction thermography," *IEEE Sensors J.*, vol. 17, no. 17, pp. 5637–5645, Sep. 2017.
- [29] Y. Gao *et al.*, "Electromagnetic pulsed thermography for natural cracks inspection," *Sci. Rep.*, vol. 7, no. 1, Feb. 2017, Art. no. 42073.
- [30] Z. Liu, B. Gao, and G. Y. Tian, "Natural cracks diagnosis system based on novel L-shaped electromagnetic sensing thermography," *IEEE Trans. Ind. Electron.*, early access, Nov. 15, 2019, doi: [10.1109/TIE.2019.2952782](https://doi.org/10.1109/TIE.2019.2952782).
- [31] Z. Xu, J. Fan, T. Liu, Y. Han, and H. Zhang, "Calcination induced phase transformation in MnZn ferrite powders," *J. Alloys Compounds*, vol. 814, Jan. 2020, Art. no. 152307.
- [32] N. Tsopelas and N. J. Siakavellas, "Performance of circular and square coils in electromagnetic-thermal non-destructive inspection," *NDT & E Int.*, vol. 40, no. 1, pp. 12–28, Jan. 2007.
- [33] M. He, L. Zhang, W. Zheng, and Y. Feng, "Investigation on a new inducer of pulsed eddy current thermography," *AIP Adv.*, vol. 6, no. 9, Sep. 2016, Art. no. 095221.
- [34] K. A. Hansen and E. C. Weisberg, "Asymmetric induction work coil for thermoplastic welding," U.S. Patent 5444220, Aug. 22, 1995.
- [35] J. Peng, G. Y. Tian, L. Wang, Y. Zhang, K. Li, and X. Gao, "Investigation into eddy current pulsed thermography for rolling contact fatigue detection and characterization," *NDT & E Int.*, vol. 74, pp. 72–80, Sep. 2015.
- [36] R. Yang, Y. He, B. Gao, G. Y. Tian, and J. Peng, "Lateral heat conduction based eddy current thermography for detection of parallel cracks and rail tread oblique cracks," *Measurement*, vol. 66, pp. 54–61, Apr. 2015.
- [37] Y. He, G. Y. Tian, M. Pan, D. Chen, and H. Zhang, "An investigation into eddy current pulsed thermography for detection of corrosion blister," *Corrosion Sci.*, vol. 78, pp. 1–6, Jan. 2014.

- [38] Z. Q. Zhu, Y. Pang, D. Howe, S. Iwasaki, R. Deodhar, and A. Pride, "Analysis of electromagnetic performance of flux-switching permanent-magnet machines by nonlinear adaptive lumped parameter magnetic circuit model," *IEEE Trans. Magn.*, vol. 41, no. 11, pp. 4277–4287, Nov. 2005.
- [39] B. Oswald-Tranta, "Induction thermography for surface crack detection and depth determination," *Appl. Sci.*, vol. 8, no. 2, p. 257, Feb. 2018.
- [40] Y. He, R. Yang, X. Wu, and S. Huang, "Dynamic scanning electromagnetic infrared thermographic analysis based on blind source separation for industrial metallic damage evaluation," *IEEE Trans. Ind. Informat.*, vol. 14, no. 12, pp. 5610–5619, Dec. 2018.
- [41] K. Tan, X. Cheng, and J. Zhang, "Correction for incidence angle and distance effects on TLS intensity data," *Wuhan Daxue Xuebao*, vol. 42, no. 2, pp. 223–228, 2017.



Xiaofeng Li received the B.Sc. degree in automation from the Southwest University of Science and Technology, Mianyang, China, in 2017. He is currently pursuing the M.Sc. degree in nondestructive testing using induction thermography technique with the University of Electronic Science and Technology of China, Chengdu, China. His research interests include induction thermography and natural microcrack testing and evaluation.



Bin Gao (Senior Member, IEEE) received the B.Sc. degree in communications and signal processing from Southwest Jiaotong University, China, in 2005, the M.Sc. (Hons.) degree in communications and signal processing and the Ph.D. degree from Newcastle University, U.K., in 2011. He worked as a Research Associate with the Newcastle University on wearable acoustic sensor technology from 2011 to 2013. He is currently a Professor with the School of Automation Engineering, University of Electronic Science and Technology of China (UESTC), Chengdu, China. He is also a very active reviewer for many international journals and long standing conferences. He has coordinated several research projects from the National Natural Science Foundation of China. His research interests include electromagnetic and thermography sensing, machine learning, nondestructive testing and evaluation, where he actively publishes in these areas.



Zewei Liu received the B.Sc. degree in automation from Henan Polytechnic University, Jiaozuo, China, in 2017. He is currently pursuing the M.Sc. degree in nondestructive testing using induction thermography technique with the University of Electronic Science and Technology of China, Chengdu, China. His research interests include automated eddy current thermography and fatigue damage testing and evaluation.



Gui Yun Tian (Senior Member, IEEE) received the B.Sc. degree in metrology and instrumentation and the M.Sc. degree in precision engineering from the University of Sichuan, Chengdu, China, in 1985 and 1988, respectively, and the Ph.D. degree from the University of Derby, Derby, U.K., in 1998. From 2000 to 2006, he was a Lecturer, a Senior Lecturer, a Reader, a Professor, and the Head of the Group of Systems Engineering, University of Huddersfield, U.K. Since 2007, he has been with Newcastle University, Newcastle upon Tyne, U.K., where he has been a Chair Professor of Sensor Technologies. He is currently an Adjunct Professor with the School of Automation Engineering, University of Electronic Science and Technology of China. He has coordinated several research projects from the Engineering and Physical Sciences Research Council (EPSRC), Royal Academy of Engineering and FP7, on top of this he also has good collaboration with leading industrial companies such as Airbus, Rolls Royce, BP, nPower, Networkrail, and TWI among others.